Exosomes are secreted at similar densities by M21 and PC3 human cancer cells and show paclitaxel solubility

William S. Fisher,[1] Christine Tchounwou,[1] Sophia Wei,[2] Logan Roberts,[2] Kai K. Ewert,[1] Cyrus R. Safinya[1]*

[1] Materials Department, Molecular, Cellular, and Developmental Biology Department, Physics Department, and Biomolecular Science and Engineering Program, University of California, Santa Barbara, California 93106, USA
[2] Molecular, Cellular, and Developmental Biology Department, University of California, Santa Barbara, California 93106, USA

* email address: cyrussafinya@ucsb.edu

Abstract

Exosomes are cell-secreted vesicles less than ≈150 nm in size that contain gene-encoding and gene-silencing RNA and cytosolic proteins with roles in intercellular communication. Interest in the use of exosomes as targeted drug delivery vehicles has grown since it was shown that they can bind specific cells and deliver intact genetic material to the cytosol of target cells. We isolated extracellular vesicles (EVs), consisting of a mixture of exosomes and microvesicles, from prostate (PC3) and melanoma (M21) cancer cell lines using serial ultracentrifugation. Interrogation via western blot analysis confirmed enrichment of CD63, a widely recognized EV surface protein, in the EV pellet from both cell lines. Nanoparticle tracking analysis (NTA) of EV pellets revealed that the two cell lines produced distinct vesicle size profiles in the ≈30 nm to ≈400 nm range. NTA further showed that the fraction of exosomes to all EVs was constant, suggesting cellular mechanisms that control the fraction of secreted vesicles that are exosomes. Transmission electron microscopy (TEM) images of the unmodified PC3 EVs showed vesicles with cup-like (i.e., nanocapsule) and previously unreported prolate morphologies. The observed non-spherical morphologies for dehydrated exosomal vesicles (size ≈30-100 nm) are most likely

related to the solid-like dense packing of proteins in exosome membranes. Solubility phase diagram data showed that EVs enhanced the solubility of paclitaxel (PTX) in aqueous solution compared to a water-only control. Combined with their inherent targeting and cytosol delivery properties, these findings highlight the potential advantages of using exosomes as chemotherapeutic drug carriers *in vivo*.

Keywords

Exosomes; Liposomes; Lipid membrane; Kinetic phase diagram; Paclitaxel membrane solubility; Drug delivery

Abbreviations

DIC, differential interference contrast microscopy; DMSO, dimethyl sulfoxide; DOPC, 1,2-dioleoyl-*sn*-glycero-3-phosphatidylcholine; DOTAP, 1,2-dioleoyl-3-trimethylammonium propane; EV, extracellular vesicles; CM, conditioned media containing EVs (exosomes and microvesicles); ILV, intraluminal vesicles; LE, late endosome; M21, human melanoma cancer; MVB, multivesicular bodies; NTA, nanoparticle tracking analysis; PBS, phosphate buffered saline; PC3, human prostate cancer; PTX, Paclitaxel; TEM, transmission electron microscopy

1. Introduction

Exosomes are a class of endogenous vesicles (or liposomes) generated and secreted by most cells. They were first identified through independent studies on trafficking of transferrin, an iron-transporting glycoprotein, in mammalian reticulocytes by the Johnstone and Stahl groups in 1983 [1,2]. The studies revealed the presence of multivesicular bodies (MVBs) within the cytosol, which contained intraluminal vesicles approximately 50 nm in size. The vesicles were observed in extracellular space following fusion of MVBs with the plasma membrane and were thus termed 'exosomes' [3].

Exosome formation starts with the process of endocytosis, where extracellular material is engulfed by the plasma membrane, which invaginates into the cytosol until it pinches off near the plasma membrane to form a new, intracellular vesicle (Figure 1). Recently formed intracellular vesicles are shuttled to the early endosome (EE, Figure 1), a large vesicle located at the periphery of the cell that is responsible for sorting internalized material prior to its transport to a specified cellular location. Following sorting in EEs, internalized material is either recycled to the plasma membrane or retained in the endosome, which matures into a late endosome (LE). This maturation involves the acidification of endosomes by membrane-bound proton pumps and the simultaneous invagination of the endosome membrane to form intraluminal vesicles (ILVs, Figure 1), which gives LEs the name multivesicular bodies (MVBs, Figure 1). Because of this mechanism of formation, ILVs naturally contain cellular proteins, nucleic acids, and other small molecules and ions. The majority of MVBs are shuttled to the acidic lysosome (pH 4.8). There, they fuse and deposit their contents, including ILVs, to be enzymatically degraded in the lumen of the lysosome. In contrast to this canonical pathway, a fraction of MVBs are shuttled to the plasma membrane, where they fuse and release their ILV content into extracellular space. The

externalized ILVs are called exosomes (Figure 1), whose functions in inter-cellular communication, many of which remain to be elucidated, extend beyond the cell where they were created.

From the formation process outlined in Figure 1 it is evident that the membrane of exosomes contains components derived from the plasma membrane [4]. Furthermore, because of the double invagination process in exosome biogenesis, some components of the outer/inner membrane layers of exosomes are derived from the corresponding outer/inner layers of plasma membranes. For example, components of lipid rafts such as glycolipids and cholesterol, as well as membrane proteins such as CD63 (which acts as a transport regulator for numerous membrane-bound proteins and influences a diverse set of cellular activities [5]), are shared between the outer layer of exosomes and plasma membranes.

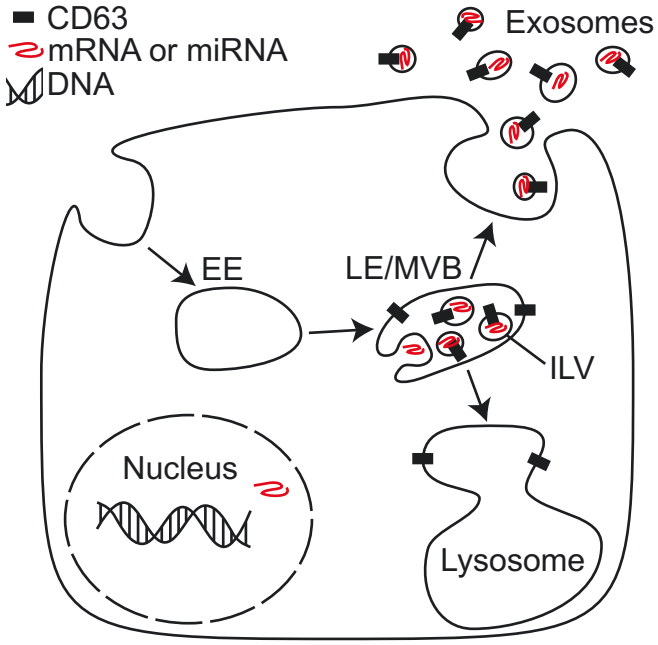

Figure 1. Exosome Biogenesis. After endocytosis and transition from early endosome (EE) to late endosome (LE), invagination of the LE membrane leads to formation of multivesicular bodies (MVB) containing intraluminal vesicles (ILVs or pre-exosomes). Secreted ILVs are termed exosomes; they are packed with nucleic acids and decorated with certain plasma membrane proteins.

Exosomes are involved in transfer of functional miRNA and mRNA, from donor to acceptor cells, that alter gene expression of target (acceptor) cells, often in a cell-specific manner [6,7,8,9,10]. The exosome-mediated modification in target cells may lead to a diverse set of regenerative and pathophysiological outcomes. For example, exosomes derived from mesenchymal stem cells are capable of reducing the inflammatory response in damaged lung tissue [11]. In contrast, cancer cell exosomes are involved in the transfer of chemotherapeutic resistance [12] as well as the induction of neoangiogenesis in human endothelial cells [13].

The biological function of exosomes suggests that they execute signaling at least in a paracrine fashion, between specific cells within a given organ, and potentially in a systemic manner, from cells in one organ to a particular cell type in another organ. It is well known that exosomes are present in a variety of bodily fluids, such as urine and blood [14], suggesting that systemic exosome release does occur. Further, variations in the protein, lipid, and glycan content of the membranes of exosomes alter their biodistribution and binding properties to target specific organ and cell types [15,16,17], suggesting naturally occurring cell specificity. However, this specificity may not be a universal property of exosomes and instead depend on the parent cell source [18]. Upon arriving at their target cell, exosomes enter the cell via endocytosis and release their content to the cytosol subsequent to fusion with the luminal membrane of cytosolic vesicles [7,19]. The underlying mechanism driving this fusion process is not well understood, though it may be facilitated by specific surface protein interactions dependent on the acidic conditions present in endocytic compartments [7,10,20]. Alternatively, key lipids within the heterogeneous lipid population of exosomal membranes may also play an essential role in the fusion process [4]. Taken together, existing evidence points to exosomes being capable of cell-specific binding

in vivo and endosomal escape upon entering target cells, properties which lend well to their use as drug delivery vehicles [6,15,19].

Liposomes are currently the most extensively studied vectors (carriers) of hydrophobic and hydrophilic drugs [21,22,23,24,25,26]. Well-known liposome formulations such as Doxil and Myocet, with chemotherapeutic payloads encapsulated in their hydrophilic interior, are in widespread clinical use [27]. Nevertheless, most liposomal vectors struggle with two major barriers: achieving targeted, cell-specific delivery *in vivo* and endosomal escape of the entrapped drug-loaded vector [28,29]. As a result, exosomes, which are potentially capable of encapsulating polar and nonpolar therapeutic molecules [19,30,31,32], have garnered significant interest in the drug delivery field because of their natural cell specificity and endosomal escape properties. Furthermore, being biologically derived, exosomes are inherently biocompatible and multiple early phase clinical trials point to their good overall safety profile [19], even though they may be weakly immunogenic because of exposed proteins at their surface. Bolstering their natural capacities, exosomes can be engineered to enhance existing targeting or to target cells they would not normally target [15]. Thus, suitably modified exosomes, which constitute a novel class of cell-derived surface-decorated liposomal vectors with a narrow size distribution between 30 nm and 150 nm, are expected to have high potential in nanomedicine therapeutics.

Drug loading capacity of a vector is a key factor in cancer cell cytotoxic efficacy [25]. The current study was designed, in part, to assess the drug loading properties of wild-type exosomes and in particular, their ability to load the cancer chemotherapy drug paclitaxel (PTX). PTX is a potent hydrophobic chemotherapeutic drug for the treatment of ovarian, breast, and non-small cell lung cancers [33,34,35,36,37,38]. The poor water solubility of PTX necessitates the use of a carrier to deliver the drug to its target cell. Taxol®, a formulation of PTX in a 1:1

mixture of polyoxyethylated castor oil and ethanol, was the most prominent PTX formulation in clinical use until 2010 [39]. Taxol is associated with severe PTX-independent hypersensitivity, which has prompted extensive research to develop safer carriers of PTX [34,40,41]. Liposomes, which solubilize PTX in their hydrophobic lipid bilayers, have emerged as major PTX delivery vectors, with liposome-PTX formulations in ongoing clinical trials in the U.S. and Taiwan [42,43]. Given the physical similarities of exosomes and liposomes, exosomes are expected to solubilize PTX in aqueous solution.

The present study sought to (i) establish a detailed and robust procedure for extracellular vesicle (EV, consisting of a mixture of exosomes and microvesicles) isolation, (ii) compare the physical properties of EVs derived from prostate cancer (PC3) and melanoma (M21) cell lines, and (iii) assess the PTX loading capacity of wild-type EVs. While exosomes are typically in the 30 to 150 nm range, microvesicles are vesicles with a wide distribution of diameters in the 100 to 1000 nm range, which pinch off from the surface of cells in a regulated process. We incubated cultured PC3 or M21 cell monolayers in exosome-depleted media to create conditioned media (CM) containing EVs and then used serial differential ultracentrifugation to isolate the EVs from the CM. The EV pellets (termed CM pellets) were obtained from the media after the final centrifugation step. These pellets were either subjected to filtration (200 nm pore size) or taken directly for content analysis.

To assess the success of our isolation procedure, we employed four assays indicative of exosome enrichment. First, nucleic acid and protein content of CM pellets isolated from PC3 and M21 CM were measured spectrophotometrically. Non-reducing western blot and protein gel analysis of the isolated PC3 and M21 CM pellets were used to assess the relative amounts of CD63 in the pellet compared to parent cells. CD63 is a known EV surface protein whose

enrichment is used as a marker [44,45]. Transmission electron microscopy (TEM) was used to image the PC3 CM pellet to assess the morphology and obtain a size estimate for the PC3 EVs. To quantitatively measure the size distribution of EVs from the isolated PC3 and M21 CM pellets, we used nanoparticle tracking analysis (NTA). The NTA data allowed us to compare the size distribution and quantity of EVs produced by PC3 and M21 cells. To test the drug loading capacity of isolated EVs, we used differential interference contrast (DIC) microscopy to visualize PTX crystallization and thus assess solubility of PTX when incubated with EVs.

The EV isolation procedure we adopted generated visible pellets which contained high concentrations of nucleic acids and protein relative to the CM supernatant. Non-reducing western blot and protein gel experiments showed enrichment of the EV surface marker CD63 in the PC3 and M21 CM pellet relative to the parent cell lysate. Remarkably, TEM images of dehydrated exosomes ≈30 to ≈100 nm in size from the pellet derived from PC3 CM revealed non-spherical (cup-like and prolate) vesicle morphologies suggestive of high-density packing of proteins within the membrane of exosomes. (Vesicles with lipids in the chain melted phase would tend to show surface roughness and protrusions upon dehydration.) NTA measurements of pellets derived from PC3 and M21 CM with and without filtration revealed EV size distributions with > 95% and > 51% of EVs between 30 and 200 nm in diameter, respectively. A surprising finding was that despite differences in concentration of vesicles in PC3 and M21 CM pellets, the fraction of exosomes, i.e. of vesicles with a size between 30 and ≈ 150 nm, was very similar between the two cell types.

Our analysis of their PTX loading capacity showed that EVs stably solubilized up to 20 μM PTX in aqueous solution for 24 h, whereas water alone only solubilized up to 10 μM

PTX over the same time period. The improved PTX solubility observed for EVs is encouraging evidence in support of exosomes as a viable drug delivery platform.

2. Materials and Methods

2.1 Materials

Stock solutions of DOTAP and DOPC in chloroform were purchased from Avanti Polar Lipids. A stock solution of PTX in DMSO was prepared by dissolving solid PTX (Acros Organics) in DMSO at 10 mM. Other chemicals were purchased from Aldrich or Fisher Scientific and used as received.

2.2 Cell culture

The human prostate cancer cell line PC3 (ATCC number: CRL-1435) and human melanoma cell line (M21) were generously donated by the Ruoslahti Lab (Sanford Burnham Prebys Medical Discovery Institute, La Jolla). M21 cells are a subclone of the human melanoma line UCLA-SO-M21 derived in the lab of Dr. R. Reisfeld (Scripps Institute, La Jolla) and originally provided by Dr. D. L. Morton (UCLA, Los Angeles). Cells were cultured in DMEM (Invitrogen) supplemented with 10% v/v fetal bovine serum (FBS; Gibco) and 1% v/v penicillin/streptomycin (Invitrogen). Cells were cultured in T75 flasks (Corning) at 37°C in a humidified incubator with 5% CO_2 and split at a 1:5 ratio after reaching ≥80% confluency (every 48–72 h) during maintenance and expansion.

2.3 Extracellular vesicle (EV) isolation

Exosomes have been found in fetal bovine serum (FBS) [46], meaning that FBS must be depleted of exosomes prior to exosome conditioning to ensure that isolated EVs originate from the intended cell source (see Figure S1 (parts A,C) in the Supplementary Information).

Successful isolation of EV pellets requires high volumes, around 200 mL, of conditioned media (see Figure S1). Thus, exosome-depleted FBS should be prepared at sufficient volumes to supplement at least 200 mL of media before executing the isolation protocol. Exosome-depleted media was prepared by centrifuging FBS at 100,000 x *g* for 18 h and retaining the top layer (light yellow versus darker red, see Figure S1 (parts A,C)). This top layer was added to DMEM (Invitrogen) to a final concentration of 10% v/v exosome-depleted FBS and 1% v/v penicillin/streptomycin (Invitrogen). Cells were expanded into 20 flasks and allowed to reach confluency, at which point the media was replaced with exosome-depleted media at 10 mL per flask and incubated for 48 h. The resulting CM was collected into four 50 mL conical tubes (Falcon) and centrifuged at 300 x *g* for 10 min at 4°C in a Sorvall RC-5 Centrifuge with a SS-34 rotor. The supernatant was collected and transferred to a new set of 50 mL conical tubes while the pellet was retained for spectrophotometric analysis or discarded. This supernatant was centrifuged at 2,000 x *g* for 30 min at 4° C, also in a Sorvall RC-5 Centrifuge with a SS-34 rotor. Next, the supernatant was again centrifuged at 10,000 x *g* for 30 min at 4°C, also in a Sorvall RC-5 Centrifuge with a SS-34 rotor, and the supernatant was transferred to 8 poly(carbonate) ultracentrifuge tubes (26.3 mL, Beckman Coulter) while the pellet was retained for spectrophotometric analysis or discarded. The supernatant was centrifuged at 100,000 x *g* for 70 min at 4°C in a Beckman Coulter Optima XL-90K centrifuge with a 50.2Ti rotor, and the supernatant was discarded while pellets were resuspended in 3 mL PBS and combined into a new ultracentrifuge tube. The resuspended pellet was centrifuged again at 100,000 x *g* for 70 min at 4°C and the supernatant was retained for spectrophotometric analysis or discarded. The pellet was resuspended into 100 μL of PBS for spectrophotometric analysis, after which an additional 400 μL of PBS were added for a total resuspension volume of 500 μL. FBS EV pellets were

obtained by diluting FBS depleted of exosomes using the method above and untreated FBS in DMEM to 10% v/v and then using 50 mL of these FBS-supplemented media as input for EV isolation, also described here. Resulting EV pellets were resuspended in 125 μL PBS for NTA analysis.

2.4 Spectrophotometric Analysis

For spectrophotometric analysis, the pellets obtained after centrifugation at 300 and 10,000 x *g* were resuspended into 3 and 2 mL PBS, respectively. Following the second centrifugation at 100,000 x *g*, 5 mL of the supernatant was removed from the top of the ultracentrifuge tube and retained. This was repeated for three additional layers of the supernatant, up to a total of 20 mL of supernatant. The remainder (≈5 mL) of the supernatant above the pellet was split into 1 mL aliquots in a similar manner (see also Figure S3 in the Supplementary Information). Dilutions (1:2 and 1:4) of the resuspended 100,000 x *g* pellet were made in PBS for spectrophotometric analysis. A total of 1.5 μL of each supernatant layer and resuspended pellet sample (see Figure S3) was used to measure absorbance at 260 and 280 nm with a NanoDrop 1000 Spectrophotometer (Thermo Fisher Scientific) to determine the estimated RNA and protein content using the instrument's software.

2.5 Western Blotting

For Western blotting, the resuspension of the EV pellet or the resuspension of the pellet obtained after centrifugation at 300 x *g* (see NTA) was used undiluted, diluted 1:2 in PBS, or diluted 1:4 in PBS. Spectrophotometric measurement showed the protein content in undiluted, samples was approximately 6.57 mg/mL and 6.58mg/mL for the 100 μL resuspension of the EV and full resuspension of the 300 x *g* pellets, respectively. A total of 12 μL of the 500 μL EV resuspension and full 300 x *g* resuspension samples were mixed with 4 μL of 4x non-reducing

loading buffer (Morris formulation, no DTT or β-mercaptoethanol) and denatured at 70°C. Denatured samples were run on two freshly prepared 10% polyacrylamide gels at 120 V for 1 h. One gel was stained overnight with Coomassie Blue dye while the other was transferred to a nitrocellulose membrane at 50 V for 2 h. The nitrocellulose membrane was blocked with 5% w/v non-fat dry milk in PBS at 4 °C for 1 h and then incubated with primary antibody (anti-CD63: Invitrogen, 10628D, 1:500) in 5% w/v non-fat dry milk in 1x PBS at 4°C overnight. After washing three times with PBS + 0.1% v/v Triton X-100 for 10 min at room temperature, the membrane was incubated with secondary antibody (IRDye® 680RD goat anti-mouse: Licor, 925-68070, 1:10,000) in 5% w/v non-fat dry milk in PBS at 4 °C for 1 h. The nitrocellulose membrane was again washed three times with PBS + 0.1% Triton X-100 for 10 min at room temperature and then imaged with an infrared imager (LI-COR Odyssey 9120 Imaging System) along with the Coomassie Blue-stained gels.

2.6 TEM

For TEM, a total of 4 μL of the undiluted, unfiltered resuspension of the PC3 CM pellet was fixed with 1 μL of a solution of 1% v/v glutaraldehyde in deionized water (0.2% glutaraldehyde final), applied to grids (200 mesh formvar/carbon/copper, Electron Microscopy Sciences), and stained with 1% w/v uranyl acetate in deionized water. TEM grids were imaged at 100,000× magnification using a JEOL 1230 transmission electron microscope (80 kV) and AMT image capture software. Image J (Fiji distribution) was used to apply a scale bar to the image and measure individual particle sizes (Analyze→Set Scale, Measure tools).

2.7 DIC Microscopy

For DIC microscopy, a total of 1 μL of a 500, 400, 300, 200, 150, or 100 μM solution of PTX in DMSO was added to 9 μL of an unfiltered suspension of CM pellet diluted to $\approx 10^{11}$

particles/mL (per NTA) in deionized water, or deionized water alone in small PCR tubes. These samples were incubated for 24 h at room temperature before imaging. After incubation, 1 μL aliquots were placed on glass microscope slides and covered by a coverslip kept in place by parafilm cutouts. These slides were imaged at 20× magnification on an inverted Diaphot 300 microscope (Nikon). The kinetic phase diagrams of PTX solubility are based on the results of two independently prepared samples.

2.8 Nanoparticle tracking analysis

For NTA samples, the unfiltered 500 μL resuspension of the CM pellet was diluted 1:500 in DI water and measured directly or filtered with a 200 nm polyethersulfone filter. These dilutions yielded total particle concentrations of 5.4×10^{11} to 1.1×10^{12} particles/mL. FBS-derived EV pellets were diluted 1:100 in DI water and measured directly and yielded 1.1×10^{10} and 7.1×10^{10} particles /mL for depleted and untreated FBS, respectively. "Sonicated liposomes" were prepared by combining a 1:1 molar ratio of DOPC and DOTAP in chloroform:methanol (3:1, v/v) at 1 mM total concentration in a small glass vial. The chloroform:methanol solvent was evaporated for 10 min under a nitrogen stream and the lipid was further dried in a vacuum for 16 h. The resultant film was resuspended in deionized water (18.2 MΩ cm) to 1 mM total concentration. This suspension was sonicated for 7 minutes with a tip sonicator (Sonics and Materials Inc. Vibra Cell, 30 Watt output) to form small unilamellar vesicles. This sample was diluted 1:1,000 in deionized water. Nanoparticle tracking analysis (NTA) of samples was performed using the NanoSight NS300 system (Malvern) and the associated NTA 3.0 analytical software (Malvern). Acquisition and analysis settings were kept constant between measurements, and scattering mode was used for NTA. The concentration of particles with 0 to 1000 nm diameter was recorded in 5 nm bins, with the reported size (diameter) at the center of each bin.

After measurement, we determined the average number of valid tracks across three technical replicates, defined as ten captures of 60 s length of a given biological replicate or stock of EV isolate. The number of valid tracks was 3901 ± 240 and 5962 ± 33 for unfiltered PC3 EV samples 1 and 2, and 4179 ± 69 and 7914 ± 110 for filtered PC3 EV samples 1 and 2. Likewise, the average number of recorded tracks was 4791 ± 165 and 6253 ± 95 for unfiltered M21 EV samples 1 and 2, and 4925 ± 363 and 3379 ± 65 for filtered M21 EV samples 1 and 2. These data were exported to Excel, where concentration was multiplied by the total dilution factor prior to measurement to obtain the concentration that was present in the original resuspension or formulation of EVs or liposomes, respectively. After adjusting for dilution, the average concentration of particles across three technical replicates was found for each of the two biological replicates from PC3 and M21 cells. Standard deviation and range were determined for each biological replicate, and the standard error across the three technical replicates was determined for the average concentration of each biological replicate. Total particle counts were calculated by multiplying the adjusted concentration of particles in each 5 nm bin by the original resuspension volume and then taking the sum of each 5 nm bin within the 0 to 30 nm, 30 to 100 nm, 100 to 200 nm, 200 to 250 nm, and 250 to 1000 nm size ranges. The number of particles in these size ranges were then expressed as fractions of the total number of particles in each whole sample (particles with 0 to 1000 nm diameter). To estimate impurities from EVs remaining in depleted FBS, the concentration of particles in the EV sample derived from depleted FBS was divided by the concentration of all particles in each cell-derived EV sample and the average and standard error of these estimates was determined.

3. Results and Discussion

3.1 Protein and RNA content of EVs isolated from cell culture

To isolate EVs from adherent cells, we used a method of differential centrifugation, synthesizing and combining methods described previously [47,48,49]. A detailed outline of the EV isolation protocol with our modifications, including a flowchart and photographs of key steps and features is shown in Figure S1 in the Supplementary Information. The procedure generated visible pellets after centrifugation at 300 and 10^5 x *g*, as identified by circles in Figure S1, parts E and F and Figure S1, parts G and H (also Figure 2, parts E and F), respectively. These visible pellets can be used as markers of progress during the isolation procedure and indicate that sufficient starting material was used to obtain a concentrated EV sample. While useful, these markers may not always be present, as variation in the amount of EV produced by different cell types may result in an invisible pellet after the final centrifugation step. We used this protocol to generate concentrated samples of EVs from the human M21 (melanoma) and PC3 (prostate cancer) cell lines. Pellets produced by these cell lines were similar upon visual inspection and quantitative measurements of particle concentration (see below) show that similar, but not equal, quantities of EVs were produced by M21 and PC3 cells.

Exosomes are expected to contain high concentrations of membrane and cytosolic proteins in addition to nucleic acids (mRNA and miRNA). As a rapid and convenient means to verify that the vesicles isolated by our protocol contained high concentrations of proteins and nucleic acids, we compared the absorbance at 260 nm and 280 nm of resuspended PC3 CM pellet samples to that of their parent cells and other fractions of the CM supernatant from which they were isolated. Supernatant fractions contained at most 12.7 ng/μL RNA and 0.15 mg/mL protein, and less than 2.5 ng/μL RNA and 0.08 mg/mL protein in all but the two most

concentrated fractions, compared with 323.2 to 358.5 ng/μL RNA and 6.58 to 6.57 mg/mL in the 300 x *g* and 10^5 x *g* pellets, respectively. Figure S3 in the Supplementary Information illustrates the fractioning of the supernatant (see also the Materials and Methods section) and compiles the spectrophotometrically determined RNA and protein concentrations for each supernatant fraction and pellet.

The resuspension of the pellet obtained after centrifugation at 10^5 x *g*, which was expected to contain exosomes, indeed contained higher (at least 28-fold) concentrations of RNA and protein than the CM supernatant from which it was isolated, suggestive of successful isolation of exosomes. The resuspensions of the pellets obtained after centrifugation at 300 and 10,000 x *g*, which contain parent cell material and apoptotic bodies and larger vesicles, respectively [48], also had relatively high RNA and protein content compared to the CM supernatant, as expected.

To confirm the presence of EVs in the isolated PC3 and M21 CM pellet, we used denaturing, non-reducing Western blotting analysis to qualitatively compare the amount of CD63 in the PC3 and M21 CM pellet versus the parent cells. It is important to note that antibodies specific for CD63 bind to an epitope containing a disulfide bond. Their binding is dependent on that bond remaining intact and therefore requires non-reducing conditions (i.e. a buffer without DTT or β-mercaptoethanol) [50]. Figure 2 shows denatured samples of the PC3 and M21 CM pellets and cells stained for CD63 (Figure 2A,B) and all protein content (Figure 2C,D). CD63 appeared as a diffuse band between 30 to 50 kDa for the CM pellets and 30 to 40 kDa for the cells. This range of observed sizes reflects a polydisperse protein, likely because CD63 is glycosylated to differing extents during synthesis [51]. The CD63 content in the PC3 and M21 CM pellet (Figure 2A,B, left three columns) was high, while it was low in the PC3 and M21 cell

samples (Figure 2A,B, right three columns). Total protein content, however, was low in the PC3 and M21 CM pellets (Figure 2C,D, left three columns) compared to the PC3 and M21 cell sample (Figure 2C,D, right three columns). Despite the much lower protein content loaded in EV versus cell lanes, CD63 content was much higher in the EV lanes. Thus, our data indicates enrichment of CD63, a known EV marker [44,45], in the PC3 and M21 CM pellet, providing evidence of successful EV isolation.

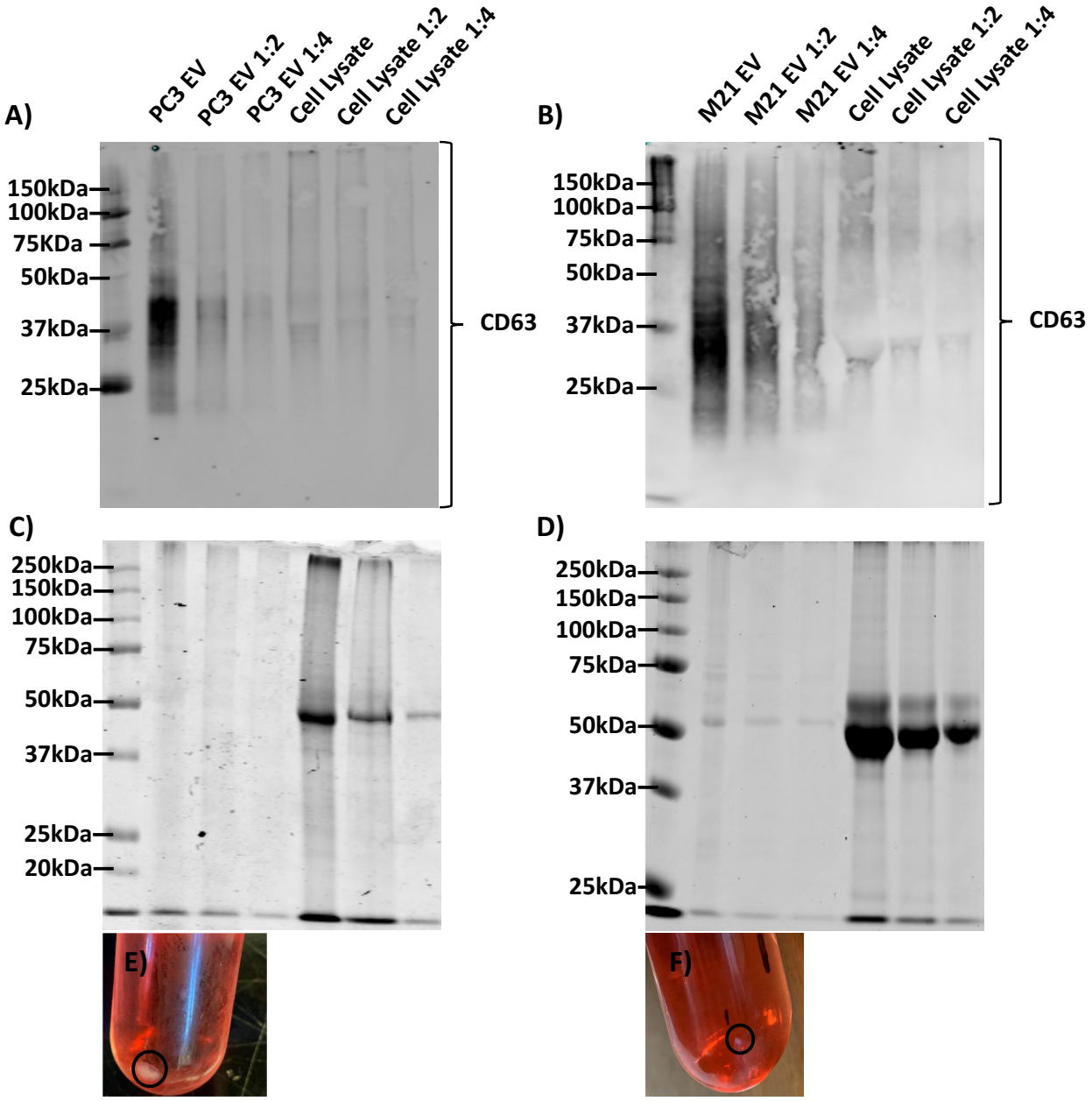

Figure 2. Protein expression analysis. Following non-reducing SDS-PAGE, we assessed protein expression using Western blot (A,B) and Coomassie Blue stain (C,D) analysis of the unfiltered PC3 and M21 CM pellet and cell lysate sample, undiluted and at 1:2 and 1:4 dilutions in PBS. The protein concentration of the input samples was decreased by the factor of the listed dilution starting at 1.31 mg/mL and 6.58 mg/mL for the EV and 300 x *g* pellets, respectively, as measured spectrophotometrically (see Figure S2 in the Supplementary Information). The resuspended CM pellet for both cell types showed much higher CD63 content in the Western blot (A,B, left three lanes) than the cell lysate (A,B, right three lanes). However, in the same region of molecular weight, the EV sample had much lower total protein content (C,D, left three lanes) than the cell lysate (C,D, right three lanes) as revealed by the Coomassie Blue stain. Together these data demonstrate CD63 enrichment in CM pellet versus parent cells. Images of PC3 (E) and M21 (F) CM pellets prior to washing are shown here and in the context of isolation in Figure S1 in the Supplementary Information. The PC3 CM pellet was used in western blotting after washing.

3.2 Distinct size profiles and densities of vesicles secreted by PC3 and M21 cells

We measured the distribution of the size, defined as vesicle diameter, of EVs in diluted samples of the PC3 and M21 CM pellets by nanoparticle tracking analysis (NTA) and compared the observed size ranges to reported values. These diluted samples were either analyzed directly or after filtration (200 nm pore size), to parse the effects of filtration. To determine the relative amount of vesicles present as a result of impurities from FBS in the culture media, we used the EV-depleted medium that PC3 and M21 cells were cultured in as the input to an isolation and measured the content of EVs in the resultant pellet by NTA (Figure S2). Comparing the total number of vesicles in EV samples from depleted medium to EV samples derived from PC3 and M21 cells, we estimate that on average 1.4 ± 0.2 % of vesicles identified in the cell-derived EVs were the result of impurities from the FBS. A control sample of cationic liposomes (CLs), consisting of a 1:1 mixture of the univalent cationic lipid DOTAP and the neutral lipid DOPC was also analyzed to validate NTA against other techniques. The DOTAP/DOPC CLs were sonicated to create a narrow size distribution with an average size below 200 nm (as measured by

Dynamic Light Scattering [25]). Figure 3 shows the concentration of EVs plotted against EV size for PC3 CM pellet samples (Figure 3A,C), M21 CM pellet samples (Figure 3B, D), and, for comparison, both CM pellet samples as well as control CLs (Figure 3E). The average size of EVs in the unfiltered PC3 CM versus filtered PC3 CM pellet samples was 179.0 ± 1.7 nm and 210.7 ± 0.4 nm versus 123.6 ± 2.4 and 115.1 ± 0.6 nm, while the average size of EVs in unfiltered versus filtered M21 CM pellet samples was 216.7 ± 3.2 nm and 172.1 ± 0.7 nm versus 121.1 ± 1.6 nm and 128.6 ± 1.9 nm (Table S1). The standard deviations of the unfiltered PC3 CM pellet samples were 81.1 nm and 90.3 nm, while the standard deviations of the filtered PC3 CM pellet samples were 41.4 nm and 33.3 nm. The standard deviation of the unfiltered M21 CM pellets were 80.8 nm and 60.3 nm, while for filtered M21 CM pellets the standard deviations were 31.9 nm and 38.0 nm. This is in line with the size profile expected for exosomes, which are consistently reported as being less than ≈150 nm in diameter, while microvesicles are expected to be between 100 and 1000 nm in diameter [9,18,52,53,54]. Notably, the NTA analysis revealed the presence of discrete peaks at specific nanoparticle sizes. The presence of distinguishable peaks suggests the presence of discrete subpopulations of EVs with more narrowly defined size ranges. Following filtration through 200 nm pores, there was a clear and expected loss of peaks that were over 220 nm and, interestingly, changes in peak locations below 200 nm. In the case of the PC3 CM pellet samples, discrete peaks at EV sizes of 112.5, 132.5, and 177.5 nm present in the unfiltered sample disappeared, while peaks at 87.5 and 92.5 nm became prominent in the filtered sample. Similarly, discrete peaks of EV sizes at 127.5, 142.5, and 182.5 nm in the unfiltered M21 CM pellet-samples disappeared following filtration, while peaks at 97.5 and 107.5 nm appeared. The displacement of peaks below 200 nm following filtration may be the result of rupture of specific vesicle populations upon extrusion which then reformed at new sizes.

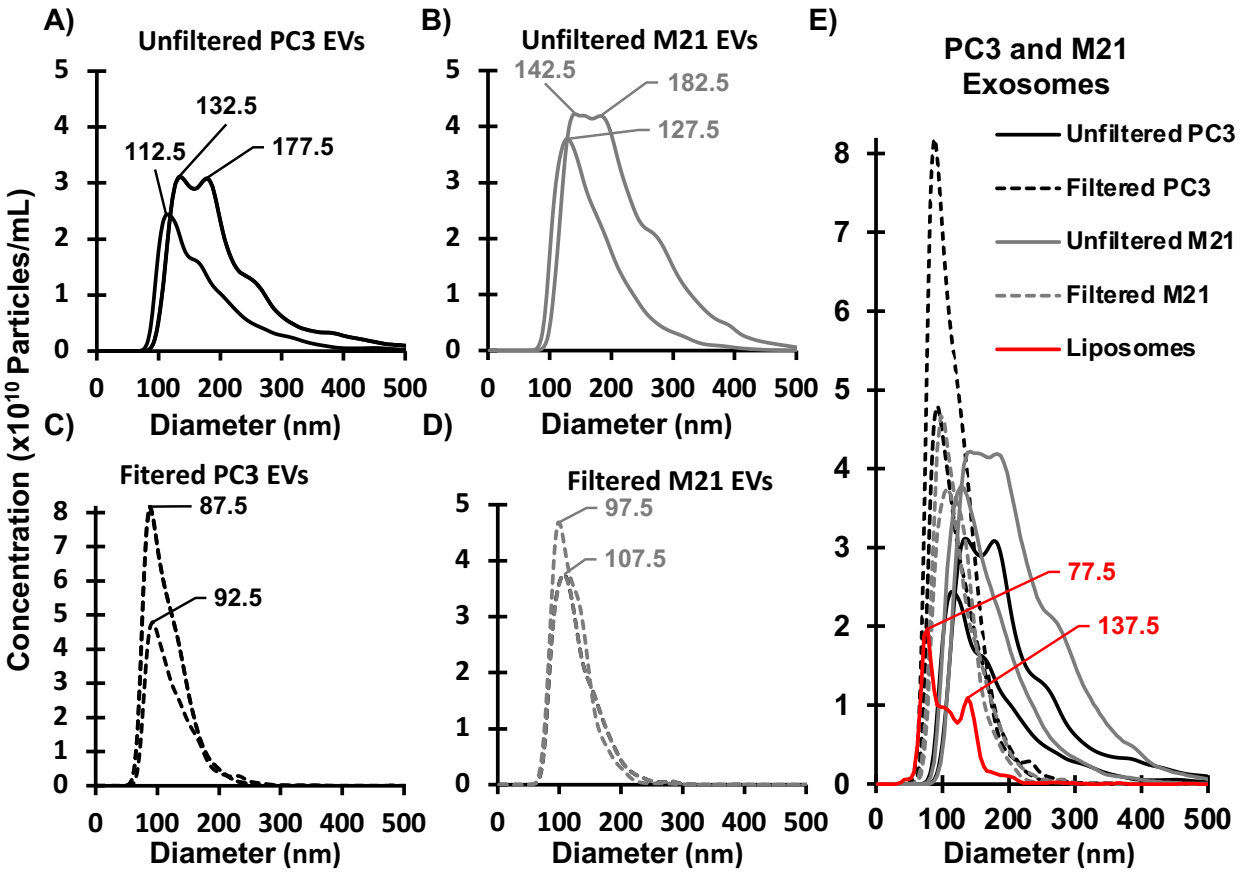

Figure 3. Nanoparticle tracking analysis. Filtered (C,D) and unfiltered (A,B) suspensions of EVs derived from PC3 (A,C) and M21 (B,D) cells were diluted in PBS and subjected to NTA to assess their size distributions in bins of 5 nm from 0 to 1000 nm. (E) An overlay of the plots of concentration (in particles/mL) over size shown in parts (A)–(D) together with the size distribution of a control sample of sonicated DOTAP:DOPC liposomes (1:1 mole ratio) at 1 mM total lipid content (red line). For this plot, the concentrations were adjusted to reflect those in the original resuspension of the CM pellets or, for liposomes, the undiluted sample. For clarity, error bars were omitted from these plots. See Figure S3 in the Supplementary Information for plots with error bars.

The NTA data showed differences in the size of major exosome subpopulations and the particle densities of exosomes produced by PC3 and M21 cells. To better understand these differences, we used the NTA data to calculate the total number of particles present in 500 μL of unfiltered and filtered PC3 and M21 CM pellet resuspensions. We then determined the

contribution of 30–100 nm, 100–200 nm, 200–250 nm, and 250–1000 nm size subpopulations to the whole population for each sample. Figure 4 visualizes this data both directly (Figure 4A) and normalized to the total number of particles (Figure 4B). The particle density of M21 CM pellet samples (Figure 4A, sixth and seventh columns) is slightly higher that of PC3 CM pellet samples (Figure 4A, second and third columns). In particular, the density of EVs with diameter 30-200 nm (the expected size range for exosomes) was 3.96×10^{11} and 3.00×10^{11} particles/mL in the unfiltered M21 CM pellet samples and 1.92×10^{11} particles/mL and 2.67×10^{11} particles/mL in the unfiltered PC3 CM pellet sample. This similarity in exosome production between cell lines is likely not limited to the cell lines we investigated, which suggests that exosomes can be isolated from a broad range of cancer cell types at similar quantities.

In addition to the similarities in particle density between the CM pellet samples derived from PC3 and M21 cells, the fraction of the total population that consisted of each distinctly sized subpopulation was very similar (Figure 4B). The nanoparticle population within the expected size range for exosomes (30–200 nm) made up around 51% and 75% versus 71% and 58% of the total population in unfiltered samples of PC3 versus M21 CM pellets (Figure 4B, second, third, sixth, and seventh columns). The 200 nm filtration increased the proportion of 30-200 nm particles up to around 95% of the total nanoparticle population for both PC3 and M21 CM pellet samples (Figure 4B, fourth, fifth, eight, and ninth columns). Ultrafiltration therefore appears effective at enriching exosomes in isolated nanoparticle samples. An alternative explanation is that aggregates of EVs were recorded as particles larger than 200 nm before filtration. Taken together, the results suggest that cells may have a mechanism that controls the fraction of secreted vesicles in the 30 to 200 nm size range.

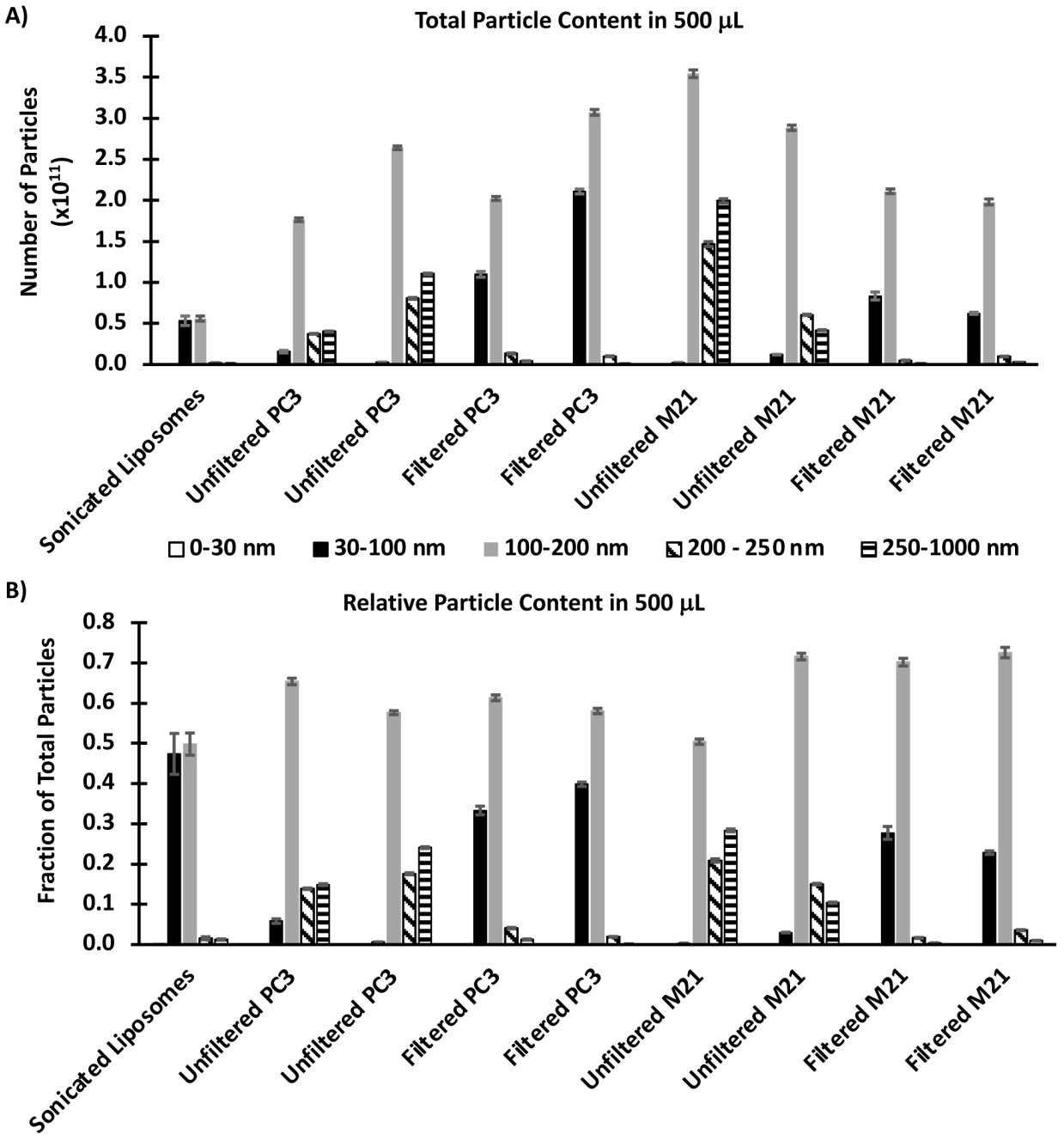

Figure 4. Nanoparticle tracking data analysis. The concentration of particles in each 5 nm bin was multiplied by 500 µL to obtain the total number of particles in the original pellet resuspension for each sample measured. The plots show **(A)** the total number of particles with diameters of 0 to 30 nm, 30 to 100 nm, 100 to 200 nm, 200 to 250 nm, and 250 to 1000 nm in each resuspension as well as the sonicated liposome sample and **(B)** the number of particles in these size groups as a fraction of the total vesicle population for each sample and the sonicated liposomes. Error bars represent standard error for measurements of each size range of a sample. This analysis shows

that M21 cells produce slightly higher but similar numbers (about 1.4 times more) of EVs than PC3 cells (part A). The ratio of particles 30 to 200 nm in size to all other particles was similar between the two cell lines, at 71 and 58% of unfiltered PC3 CM pellet samples and 51% and 75% of unfiltered M21 CM pellet samples. This ratio increased to 95% and 98% of filtered PC3 CM pellet samples and 98% and 95% of M21 CM pellet samples, respectively (part B). The high ratio of 30 to 200 nm particles suggests that exosomes were successfully isolated from both cell lines. Filtration increased the fraction of exosomes in each sample, by removing a portion of vesicles larger than 200 nm (Part B) or dispersion of EV aggregates, which is suggested by the increase in number of 30-100 nm particles (Part A).

3.3 Novel morphology of exosomes imaged with TEM

A sample of the unfiltered PC3 CM pellet was imaged at 100,000× magnification using TEM and the image was processed to analyze particle morphology and obtain size estimates. A representative image is shown in Figure 5 together with size measurements for selected nanoparticles that span the range of observed sizes. The EVs largely exhibit cup-shaped morphologies (i.e., similar to nanocapsules). Others have also reported such cup-shaped exosomes [48,55,56]. Size measurements of the PC3 CM pellet EVs in TEM images revealed diameters ranging from 20 to 100 nm, which is smaller than the range reported by NTA. This size difference may be due to a combination of aggregation of EVs during NTA measurements and the vesicle shrinkage expected when using negative staining to obtain TEM images of air-dried biological vesicles [57].

Interestingly, some of the EVs display prolate shapes. Vesicles, such as the control DOTAP/DOPC CLs, typically adopt surface tension-mediated spherical shapes, because their lipid bilayer membrane is in the fluid phase with chain-melted lipid tails (di-oleoyl (C18:1), with one *cis* double bond). Though it is not expected to be their native shape, the observation of non-spherical morphologies (i.e., the cup and prolate shapes) for the air dried EVs is consistent with

the interpretation that the exosome membranes are packed with membrane proteins, effectively placing them in a jammed state. This would result in exosomes with solid-like or glassy membranes that resist surface tension forces when wet and resist shape changes upon dehydration. We note that drying of a spherical vesicle with lipids in the chain melted phase typically leads to a shrunken vesicle with surface undulations and protrusions due to reduced internal volume of the vesicle. In contrast, the TEM image of EVs in Figure 5 reveals prolate shapes lacking surface undulations, consistent with solid-like surfaces.

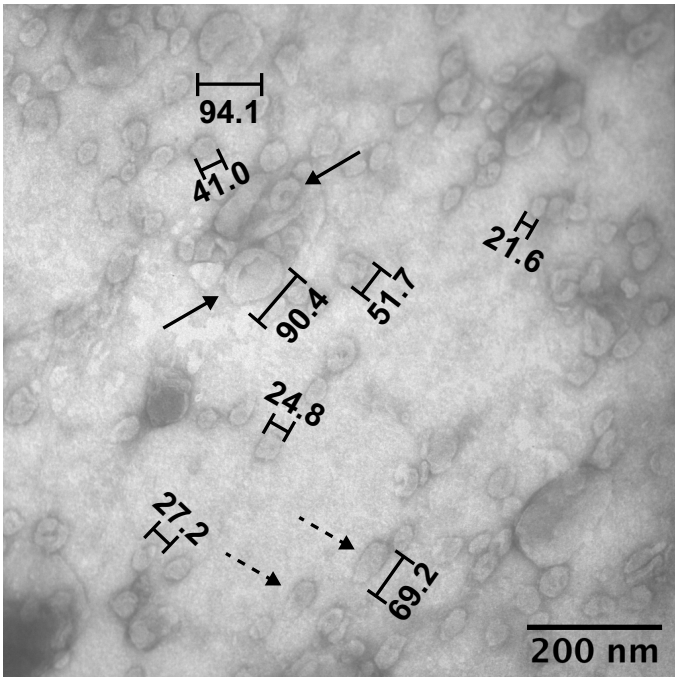

Figure 5. Transmission electron micrograph of a fixed, stained (uranyl acetate) undiluted PC3 EV resuspension. The observed sizes agree with reported exosome sizes and their cup-like morphologies (arrows with solid lines) agree with reported morphologies. However, some particles had prolate shapes (arrows with dashed lines), which is not a commonly reported feature of exosomes. The existence of clusters of particles in this image suggests that exosomes aggregate in stored samples. This may have contributed to the difference in size distribution seen in NTA versus TEM images.

3.4 Solubility of paclitaxel in EVs

Having established a detailed protocol which isolated EVs from two cell lines, we wanted to explore the potential of exosomes as drug nanocarriers. To do so, we assessed the ability of EVs derived from M21 and PC3 cells to solubilize paclitaxel (PTX) in aqueous suspension over 24 h at room temperature. The solubility behavior of PTX in EVs is important for their efficacy in drug delivery because PTX crystals, which form due to PTX self-association in the membrane followed by phase separation, are therapeutically inert [25,58].

We used differential-interference-contrast (DIC) microscopy to monitor PTX solubility through the formation of PTX crystals [25,26]. Representative DIC micrographs are shown in Figure 6A. PTX precipitated from the solution at 30 μM or greater in all samples (Figure 6A, top row), while it remained soluble at 10 μM in water (i.e., a control sample prepared by adding a PTX solution in DMSO to water), PC3 EV, and M21 EV samples (Figure 6A, bottom row). We compiled the DIC data into a concentration-dependent solubility phase diagram [25], which displays the solubilization status of various concentrations of PTX 24 h after dilution from DMSO into water containing no EVs, PC3-derived EVs, or M21-derived EVs after multiple trials. Examples of needle-shaped PTX crystals can be seen at 24 h after addition of PTX to a final concentration of 30 μM in the M21 EV sample (Figure 6A, top center panel) and PC3 EV sample (Figure 6A, top right panel). These crystals are similar to those observed in the control (plain water) sample at the same final PTX concentration (Figure 6A, top left panel). When diluted into water from DMSO solution (to a final volume ratio of water/DMSO=9:1), PTX displayed limited solubility of up to 10 μM after 24 h (Figure 6A, lower left panel, where no crystals are present and 6B, left column). We found that after 24 h, PTX remained solubilized at 15 μM in all trials with M21 and PC3 EVs, with no evidence of crystal formation (Figure 6B, center and right column). In contrast, crystals were observed in the control (water) sample at this

PTX concentration. Increasing the PTX concentration to 20 μM in the samples containing M21 EVs resulted in insolubility and crystal formation in one out of two trials after 24 h (Figure 6B, center column) but neither trial with PC3 EVs (Figure 6B, right column). Therefore, PC3-derived EVs solubilize at least 5 μM of PTX, because our data shows that the critical concentration for PTX crystallization is between 10 and 15 μM in water, while it is larger than 20 μM in water with PC3-derived EVs. Taken together, these data indicate an enhanced solubility of PTX in suspensions of M21- and PC3-derived EVs compared to water alone. NTA data suggests a very large portion of these EVs are exosomes. Given the previously discussed targeting and endosomal escape properties of exosomes, this enhanced solubilization further supports the use of exosomes as chemotherapeutic drug carriers.

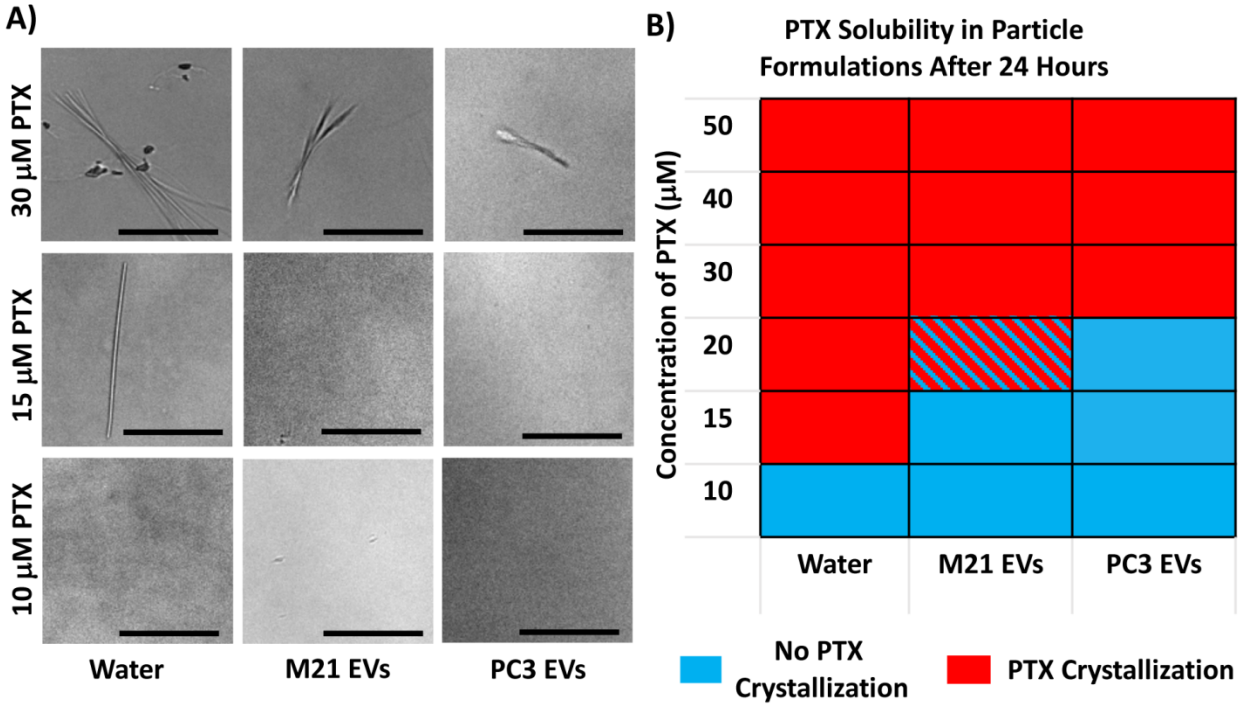

Figure 6. PTX solubility in the presence of EVs. Varied amounts of PTX, dissolved in a constant volume of DMSO, were added to water (control) or an EV sample derived from PC3 or M21 cells at a concentration of ≈10^{11} particles/mL, such that the DMSO:water ratio in the resulting samples was 1:9 (v/v). At 24 h after PTX addition, the samples were assessed for PTX crystals using differential-interference-contrast (DIC) microscopy. **(A)**

Representative DIC micrographs with (top row and left image of middle row; final PTX concentration 30 μM and 15 μM, respectively) and without (bottom row and center and right image of middle row; final PTX concentration 10 μM and 15 μM, respectively) PTX crystallization. Scale bars represent 50 μm. **(B)** Solubility phase diagram constructed from DIC microscopy data, using multiple trials for each sample. Conflicting data points are those at which PTX crystals were observed in some trials but not in others. The extended solubility window for the EV samples indicates that EVs are capable of solubilizing PTX added to an aqueous solution to a greater extent than water and DMSO.

4. Conclusions

The serial differential ultracentrifugation protocol detailed in this study generates EVs of ≈30 nm to ≈400 nm in size from two distinct human cancer cell lines, as measured by NTA and confirmed by TEM. Western blotting and TEM further demonstrated that these EVs were enriched for the EV surface protein marker CD63 and had a cup-shaped morphology characteristic of exosomes, respectively. The quantitative NTA data presented here revealed only minor differences in the quantity of EVs produced, suggesting that EVs can be isolated from diverse cell types at quantities sufficient for study and therapeutic development. In addition, the ratio of EVs 30-200 nm in size to EVs of all sizes remained nearly the same for M21 and PC3 cells, which may result from a shared cellular control mechanism governing the fraction of secreted vesicles that fall within the 30-200 nm size range. The size ranges of discrete secreted vesicle populations may be related to their intended cellular uptake route; for example, caveolar endocytosis preferentially takes in 50-100 nm size vesicles while alternate endocytic routes are used for larger vesicles.

The non-spherical (cup-like and prolate) shapes of the EVs we isolated are most likely a result of the composition of exosome membranes, which are packed with proteins. This densely

packed state would produce solid or glass-like membranes consistent with the non-spherical morphologies observed in TEM. Solubility phase diagram studies showed enhanced PTX solubilization in EVs, which were largely exosomes according to NTA data, suspended in aqueous solution. Thus, combined with the inherent targeting and endosomal escape properties of exosomes, our data provides proof-of-concept support for their use as chemotherapeutic drug carriers. Our findings pave the way for future studies on the cytotoxic efficacy of PTX-loaded exosomes against human cancer cells such as, in particular, studies toward developing an understanding of the dependence of exosome vector efficacy on the physiochemical properties of exosomes, including their size, shape, and PTX solubility properties. Understanding these relationships is crucial to the development of exosomes as chemotherapeutic drug carriers for cancer therapies.

Acknowledgements

This research study was supported by the National Institutes of Health under Award R01GM130769 (mechanistic studies on developing lipid nanoparticles for drug delivery). Partial support was provided by the US National Science Foundation (NSF) under Award DMR-1807327 (kinetic phase behavior of vesicles with hydrophobic molecules). We thank the lab of Dr. Stuart C. Feinstein (University of California, Santa Barbara) for the gift of the IRDye® 680RD goat anti-mouse antibody and other materials and assistance in running Western blotting experiments. The authors acknowledge the use of the JEOL 1230 transmission electron microscope available through the NRI-MCDB microscopy facility at the University of California, Santa Barbara. The authors further acknowledge the use of the NanoSight NS300 instrument in the Biological Nanostructures Laboratory within the California NanoSystems

Institute, supported by the University of California, Santa Barbara and the University of California, Office of the President. We thank Dr. Jennifer Smith, the manager of the Biological Nanostructures Laboratory, for assistance in conducting these measurements.

References

[1] B.T. Pan, R.M. Johnstone, Fate of the transferrin receptor during maturation of sheep reticulocytes in vitro: Selective externalization of the receptor, Cell, 33 (1983) 967–978.

[2] C. Harding, J. Heuser, P. Stahl, Receptor-mediated endocytosis of transferrin and recycling of the transferrin receptor in rat reticulocytes, The Journal of Cell Biology, 97 (1983) 329–339.

[3] R.M. Johnstone, M. Adam, J.R. Hammond, L. Orr, C. Turbide, Vesicle formation during reticulocyte maturation Association of plasma membrane activities with released vesicles (exosomes), Journal of Biological Chemistry, 262 (1987) 9412–9420.

[4] A. Llorente, T. Skotland, T. Sylvänne, D. Kauhanen, T. Róg, A. Orłowski, I. Vattulainen, K. Ekroos, K. Sandvig, Molecular lipidomics of exosomes released by PC-3 prostate cancer cells, Biochimica et Biophysica Acta - Molecular and Cell Biology of Lipids, 1831 (2013) 1302–1309.

[5] M.S. Pols, J. Klumperman, Trafficking and function of the tetraspanin CD63, Experimental Cell Research, 315 (2009) 1584–1592.

[6] H. Valadi, K. Ekström, A. Bossios, M. Sjöstrand, J.J. Lee, J.O. Lötvall, Exosome-mediated transfer of mRNAs and microRNAs is a novel mechanism of genetic exchange between cells, Nature Cell Biology, 9 (2007) 654–9.

[7] I. Parolini, C. Federici, C. Raggi, L. Lugini, S. Palleschi, A. De Milito, C. Coscia, E. Iessi, M. Logozzi, A. Molinari, M. Colone, M. Tatti, M. Sargiacomo, S. Fais, Microenvironmental pH is a key factor for exosome traffic in tumor cells, Journal of Biological Chemistry, 284 (2009) 34211–34222.

[8] M. Chivet, C. Javalet, K. Laulagnier, B. Blot, F.J. Hemming, R. Sadoul, Exosomes secreted by cortical neurons upon glutamatergic synapse activation specifically interact with neurons, Journal of Extracellular Vesicles, 3 (2014).

[9] M. Sancho-Albero, N. Navascués, G. Mendoza, V. Sebastián, M. Arruebo, P. Martín-Duque, J. Santamaría, Exosome origin determines cell targeting and the transfer of

therapeutic nanoparticles towards target cells, Journal of Nanobiotechnology, 17 (2019) 1–13.

[10] T.J. Smyth, J.S. Redzic, M.W. Graner, T.J. Anchordoquy, Examination of the specificity of tumor cell derived exosomes with tumor cells in vitro, Biochimica et Biophysica Acta - Biomembranes, 1838 (2014) 2954–2965.

[11] G.R. Willis, A. Fernandez-Gonzalez, J. Anastas, S.H. Vitali, X. Liu, M. Ericsson, A. Kwong, S.A. Mitsialis, S. Kourembanas, Mesenchymal stromal cell exosomes ameliorate experimental bronchopulmonary dysplasia and restore lung function through macrophage immunomodulation, American Journal of Respiratory and Critical Care Medicine, 197 (2018) 104–116.

[12] J. Li, X. Yang, H. Guan, A. Mizokami, E.T. Keller, X. Xu, X. Liu, J. Tan, L. Hu, Y. Lu, J. Zhang, Exosome-derived microRNAs contribute to prostate cancer chemoresistance, International Journal of Oncology, 49 (2016) 838–846.

[13] C. Grange, M. Tapparo, F. Collino, L. Vitillo, C. Damasco, M.C. Deregibus, C. Tetta, B. Bussolati, G. Camussi, Microvesicles released from human renal cancer stem cells stimulate angiogenesis and formation of lung premetastatic niche, Cancer Research, 71 (2011) 5346–5356.

[14] K. Kalishwaralal, W.Y. Kwon, K.S. Park, Exosomes for Non-Invasive Cancer Monitoring, Biotechnology Journal, 14 (2019) 1–11.

[15] D.E. Murphy, O.G. de Jong, M. Brouwer, M.J. Wood, G. Lavieu, R.M. Schiffelers, P. Vader, Extracellular vesicle-based therapeutics: natural versus engineered targeting and trafficking, Experimental and Molecular Medicine, 51 (2019).

[16] M.H. Rashid, T.F. Borin, R. Ara, K. Angara, J. Cai, B.R. Achyut, Y. Liu, A.S. Arbab, Differential in vivo biodistribution of 131I-labeled exosomes from diverse cellular origins and its implication for theranostic application, Nanomedicine: Nanotechnology, Biology, and Medicine, 21 (2019) 102072.

[17] O.P.B. Wiklander, J.Z. Nordin, A. O'Loughlin, Y. Gustafsson, G. Corso, I. Mäger, P. Vader, Y. Lee, H. Sork, Y. Seow, N. Heldring, L. Alvarez-Erviti, C.I. Edvard Smith, K. Le Blanc, P. Macchiarini, P. Jungebluth, M.J.A. Wood, S. El Andaloussi, Extracellular vesicle in vivo biodistribution is determined by cell source, route of administration and targeting, Journal of Extracellular Vesicles, 4 (2015) 1–13.

[18] T. Smyth, M. Kullberg, N. Malik, P. Smith-Jones, M.W. Graner, T.J. Anchordoquy, Biodistribution and delivery efficiency of unmodified tumor-derived exosomes, Journal of Controlled Release, 199 (2015) 145–155.

[19] O.M. Elsharkasy, J.Z. Nordin, D.W. Hagey, O.G. de Jong, R.M. Schiffelers, S. EL Andaloussi, P. Vader, Extracellular vesicles as drug delivery systems: Why and how?, Advanced Drug Delivery Reviews, (2020).

[20] E. Bonsergent, G. Lavieu, Content release of extracellular vesicles in a cell-free extract, FEBS Letters, 593 (2019) 1983–1992.

[21] C.R. Safinya, J.O. Rädler, eds., Handbook of Lipid Membranes: Molecular, Functional, and Materials Aspects. 1st ed., CRC Press, Taylor & Francis Group, Boca Raton, 2021.

[22] A.D. Bangham, R.W. Horne, Negative staining of phospholipids and their structural modification by surface-active agents as observed in the electron microscope, Journal of Molecular Biology, 8 (1964) 660–668.

[23] T.M. Allen, P.R. Cullis, Liposomal drug delivery systems: From concept to clinical applications, Advanced Drug Delivery Reviews, 65 (2013) 36–48.

[24] C.R. Safinya, K.K. Ewert, R.N. Majzoub, C. Leal, Cationic liposome-nucleic acid complexes for gene delivery and gene silencing, New Journal of Chemistry, 38 (2014) 5164–5172.

[25] V.M. Steffes, M.M. Murali, Y. Park, B.J. Fletcher, K.K. Ewert, C.R. Safinya, Distinct solubility and cytotoxicity regimes of paclitaxel-loaded cationic liposomes at low and high drug content revealed by kinetic phase behavior and cancer cell viability studies, Biomaterials, 145 (2017) 242–255.

[26] V.M. Steffes, Z. Zhang, S. MacDonald, J. Crowe, K.K. Ewert, B. Carragher, C.S. Potter, C.R. Safinya, PEGylation of Paclitaxel-Loaded Cationic Liposomes Drives Steric Stabilization of Bicelles and Vesicles thereby Enhancing Delivery and Cytotoxicity to Human Cancer Cells, ACS Applied Materials and Interfaces, 12 (2020) 151–162.

[27] A. Fritze, F. Hens, A. Kimpfler, R. Schubert, R. Peschka-Süss, Remote loading of doxorubicin into liposomes driven by a transmembrane phosphate gradient, Biochimica et Biophysica Acta - Biomembranes, 1758 (2006) 1633–1640.

[28] D. Rosenblum, N. Joshi, W. Tao, J.M. Karp, D. Peer, Progress and challenges towards targeted delivery of cancer therapeutics, Nature Communications, 9 (2018).

[29] S.A. Smith, L.I. Selby, A.P.R. Johnston, G.K. Such, The Endosomal Escape of Nanoparticles: Toward More Efficient Cellular Delivery, Bioconjugate Chemistry, 30 (2019) 263–272.

[30] T.A. Druzhkova, A.A. Yakovlev, Exosome Drug Delivery through the Blood–Brain Barrier: Experimental Approaches and Potential Applications, Neurochemical Journal, 12 (2018) 195–204.

[31] T. Yang, P. Martin, B. Fogarty, A. Brown, K. Schurman, R. Phipps, V.P. Yin, P. Lockman, S. Bai, Exosome Delivered Anticancer Drugs Across the Blood-Brain Barrier for Brain Cancer Therapy in Danio Rerio, Pharmaceutical Research, 32 (2015) 2003–2014.

[32] S.G. Antimisiaris, S. Mourtas, A. Marazioti, Exosomes and exosome-inspired vesicles for targeted drug delivery, Pharmaceutics, 10 (2018).

[33] B.A. Weaver, How Taxol/paclitaxel kills cancer cells, Molecular Biology of the Cell, 25 (2014) 2677–2681.

[34] N. Gupta, H. Hatoum, G.K. Dy, First line treatment of advancfved non-small-cell lung cancer - Specific focus on albumin bound paclitaxel, International Journal of Nanomedicine, 9 (2013) 209–221.

[35] N.C. Kampan, M.T. Madondo, O.M. McNally, M. Quinn, M. Plebanski, Paclitaxel and its evolving role in the management of ovarian cancer, BioMed Research International, 2015 (2015).

[36] Y. Zong, J. Wu, K. Shen, Nanoparticle albumin-bound paclitaxel as neoadjuvant chemotherapy of breast cancer: A systematic review and meta-analysis, Oncotarget, 8 (2017) 17360–17372.

[37] Institute for Health Metrics and Evaluation (IHME) University of Washington, GBD Compare. http://vizhub.healthdata.org/gbd-compare, 2015 (accessed 5 May 2020).

[38] J.R. Molina, P. Yang, S.D. Cassivi, S.E. Schild, A.A. Adjei, Non-small cell lung cancer: Epidemiology, risk factors, treatment, and survivorship, Mayo Clinic Proceedings, 83 (2008) 584–594.

[39] A.M. Sofias, M. Dunne, G. Storm, C. Allen, The battle of "nano" paclitaxel, Advanced Drug Delivery Reviews, 122 (2017) 20–30.

[40] C. Scripture, W. Figg, A. Sparreboom, Peripheral Neuropathy Induced by Paclitaxel: Recent Insights and Future Perspectives, Current Neuropharmacology, 4 (2006) 165–172.

[41] P. Vishnu, V. Roy, Safety and efficacy of nab paclitaxel in the treatment of patients with breast cancer, Breast Cancer: Basic and Clinical Research, 5 (2011) 53–65.

[42] J.A. Zhang, G. Anyarambhatla, L. Ma, S. Ugwu, T. Xuan, T. Sardone, I. Ahmad, Development and characterization of a novel Cremophor® EL free liposome-based paclitaxel (LEP-ETU) formulation, European Journal of Pharmaceutics and Biopharmaceutics, 59 (2005) 177–187.

[43] A. Awada, I.N. Bondarenko, J. Bonneterre, E. Nowara, J.M. Ferrero, A. V. Bakshi, C. Wilke, M. Piccart, A randomized controlled phase ii trial of a novel composition of

paclitaxel embedded into neutral and cationic lipids targeting tumor endothelial cells in advanced triple-negative breast cancer (tnbc), Annals of Oncology, 25 (2014) 824–831.

[44] J.M. Escola, M.J. Kleijmeer, W. Stoorvogel, J.M. Griffith, O. Yoshie, H.J. Geuze, Selective enrichment of tetraspan proteins on the internal vesicles of multivesicular endosomes and on exosomes secreted by human B-lymphocytes, Journal of Biological Chemistry, 273 (1998) 20121–20127.

[45] M.R. Fernando, C. Jiang, G.D. Krzyzanowski, W.L. Ryan, New evidence that a large proportion of human blood plasma cell-free DNA is localized in exosomes, PLoS ONE, 12 (2017) 1–15.

[46] G.V. Shelke, C. Lässer, Y.S. Gho, J. Lötvall, Importance of exosome depletion protocols to eliminate functional and RNA-containing extracellular vesicles from fetal bovine serum, Journal of Extracellular Vesicles, 3 (2014) 1–8.

[47] G. Raposo, W. Stoorvogel, Extracellular vesicles: Exosomes, microvesicles, and friends, Journal of Cell Biology, 200 (2013) 373–383.

[48] C. Théry, S. Amigorena, G. Raposo, A. Clayton, Isolation and characterization of exosomes from cell culture supernatants and biological fluids, Current Protocols in Cell Biology, Chapter 3 (2006) Unit 3.22.

[49] C. Lässer, M. Eldh, J. Lötvall, Isolation and Characterization of RNA-Containing Exosomes, Journal of Visualized Experiments, (2012) 1–6.

[50] E.J.K. Kowal, D. Ter-Ovanesyan, A. Regev, G.M. Church, Extracellular Vesicle Isolation and Analysis by Western Blotting, Extracellular Vesicles: Methods and Protocols, (2017) 143–152.

[51] M. Ageberg, A. Lindmark, Characterisation of the biosynthesis and processing of the neutrophil granule membrane protein CD63 in myeloid cells, Clinical and Laboratory Haematology, 25 (2003) 297–306.

[52] L. Alvarez-Erviti, Y. Seow, H. Yin, C. Betts, S. Lakhal, M.J.A. Wood, Delivery of siRNA to the mouse brain by systemic injection of targeted exosomes, Nature Biotechnology, 29 (2011) 341–345.

[53] T.S. Martins, J. Catita, I.M. Rosa, O.A.B. Da Cruz e Silva, A.G. Henriques, Exosome isolation from distinct biofluids using precipitation and column-based approaches, PLoS ONE, 13 (2018) 1–16.

[54] M. Millard, I. Yakavetsa, M. Piffoux, A. Brun, F. Gazeau, J.M. Guigner, J. Jasniewski, H.P. Lassalle, C. Wilhelm, L. Bezdetnaya, mTHPC-loaded extracellular vesicles outperform liposomal and free mTHPC formulations by an increased stability drug

delivery efficiency and cytotoxic effect in tridimensional model of tumors, Drug Delivery, 25 (2018) 1790–1801.

[55] S. Gupta, S. Rawat, V. Arora, S.K. Kottarath, A.K. Dinda, P.K. Vaishnav, B. Nayak, S. Mohanty, An improvised one-step sucrose cushion ultracentrifugation method for exosome isolation from culture supernatants of mesenchymal stem cells, Stem Cell Research and Therapy, 9 (2018) 1–11.

[56] Y. Wang, V. Balaji, S. Kaniyappan, L. Krüger, S. Irsen, K. Tepper, R. Chandupatla, W. Maetzler, A. Schneider, E. Mandelkow, E.M. Mandelkow, The release and trans-synaptic transmission of Tau via exosomes, Molecular Neurodegeneration, 12 (2017) 1–25.

[57] S. De Carlo, J.R. Harris, Negative staining and Cryo-negative Staining of Macromolecules and Viruses for TEM, Micron, 42 (2012) 117-131.

[58] S. V. Balasubramanian, R.M. Straubinger, Taxol-Lipid Interactions: Taxol-Dependent Effects on the Physical Properties of Model Membranes, Biochemistry, 33 (1994) 8941–8947.